This is an accepted manuscript version
The final paper is accessible via http://dx.doi.org/10.1016/j.jsg.2014.08.004

Strain rate dependent calcite microfabric evolution – an experiment carried out by nature

Anna Rogowitz[1*], Bernhard Grasemann[1], Benjamin Huet[1] and Gerlinde Habler[2]

[1]Department of Geodynamics and Sedimentology
University of Vienna
Althanstrasse 14
Wien, A-1090
Austria
anna.rogowitz@univie.ac.at
Phone number (Department): +43-1-4277-53462

bernhard.grasemann@univie.ac.at
benjamin.huet@univie.ac.at

[2]Department of Lithospheric Research
University of Vienna
Althanstrasse 14
Wien, A-1090
Austria
gerlinde.habler@univie.ac.at

Keywords

calcite; deformation mechanism; recrystallization mechanism; microfabric; strain localization

Abstract

A flanking structure developed along a secondary shear zone in calcite marbles, on Syros (Cyclades, Greece), provides a natural laboratory for directly studying the effects of strain rate variations on calcite deformation at identical pressure and temperature conditions. The presence and rotation of a fracture during progressive deformation caused extreme variations in finite strain and strain rate, forming a localized ductile shear zone that shows different microstructures and textures. Textures and the degree of intracrystalline deformation were measured by electron backscattered diffraction. Marbles from the host rocks and the shear zone, which deformed at various strain rates, display crystal-preferred orientation, suggesting that the calcite preferentially deformed by intracrystalline-plastic deformation. Increasing strain rate results in a switch from subgrain rotation to bulging recrystallization in the dislocation-creep regime. With increasing strain rate, we observe in fine-grained (3 μm) ultramylonitic zones a change in deformation regime from grain-size insensitive to grain-size sensitive. Paleowattmeter and the paleopiezometer suggest strain rates for the localized shear zone around 10^{-10} s^{-1} and for the marble host rock around 10^{-12} s^{-1}. We conclude that varying natural strain rates can have a first-order effect on the microstructures and textures that developed under the same metamorphic conditions.

1. Introduction

Crystal-plastic deformation of calcite has been the focus of many experimental studies. Different initial grain sizes, strain rates, stresses, temperatures, dry/wet conditions and CO_2 partial pressures have been considered to investigate a wide range of deformation regimes (e.g. Schmid et al., 1980; Schmid et al., 1987; Rutter, 1995; De Bresser and Spiers, 1997; Pieri et al., 2001; Barnhoorn et al., 2004; Barber

et al., 2007; Llana-Fúnez and Rutter, 2008; Liteanu et al., 2012; Rybacki et al., 2013). Flow laws for the dislocation and diffusion creep fields have been determined with respect to strain rates, stresses and temperatures (e.g. De Bresser et al., 2002; Renner et al., 2002; Herwegh et al., 2003). Twinning on e-planes seems to be common during deformation of calcite rocks at temperatures below 400 ℃ (Ferrill et al., 2004). For crystallographic reasons total twinning in calcite would lead to a shear strain of γ= 0.69, under the simplifying assumption that the twin plane is oriented parallel to the shear-zone boundary (Schmid et al., 1987). Therefore, increasing strain requires the additional activation of intracrystalline slip (Rybacki et al., 2013). Textures developed at small strain ($\gamma < 2$) are similar in a wide temperature range while at greater strain, textures vary with increasing temperature (Barnhoorn et al., 2004). Flow laws and deformation-mechanism maps suggest preferential deformation by grain-size sensitive mechanisms (GSS) at small grain sizes, whereas coarse-grained rocks deform by dislocation creep (Schmid et al., 1987).

Complementary to experimental studies, textural and microstructural investigations of natural calcite marbles characterized shear sense, flow type, deformation mechanisms, and pressure and temperature conditions (Vernon, 1981; Ratschbacher et al., 1991; Kurz et al., 2000; Bestmann et al., 2000; 2003; 2006; Trullenque et al., 2006; Oesterling et al., 2007; Austin et al., 2008). These studies also document a switch from twinning to dislocation creep regime with increasing strain. Recrystallization by subgrain rotation (SGR) and less common bulging (BLG) result in grain size reduction, which is often followed by the activation of GSS creep. However, a direct comparison of experimentally and naturally deformed calcite remains difficult because of the extreme difference between experimental and natural strain rates (Patterson, 1987).

In this study, we investigate deformation mechanisms within and outside the cross cutting element of a flanking structure developed in almost pure calcite marbles on Syros (Cyclades, Greece). Such a structure forms, when a planar inclusion of finite length (i.e. the cross cutting element, CE) deforms within a host rock resulting in the rotation of the CE and slip along it (Grasemann & Stüwe, 2001; Passchier, 2001). Due to the slip gradient along the CE, a heterogeneous strain field in the surrounding area causes marker layers to deform by normal and/or reverse drag (Reches and Eidelman, 1995; Passchier, 2001; Grasemann et al., 2005). Coeval with flanking fold development at low shear strain, deformation within the CE may record shear strain and strain rates, which are much greater than these background values (Grasemann et al., 2011; Fig.1). The flanking structure on Syros thus represents a natural experiment, where a specific marble was deformed at relatively small strain-rates in the host rock and at much greater strain rates within the CE under the same metamorphic conditions. The current study documents calcite microfabric evolution for natural geological conditions, providing the opportunity to study deformation and recrystallization mechanisms of calcite as a function of strain and strain rates. The consistency of experimentally determined flow laws, piezometer and paleowattmeter are tested with parameters derived from the calcite samples, which deformed under natural conditions.

2. Geological setting

The island of Syros (Greece) is part of the Cycladic blueschist belt that is situated in the back-arc of the Hellenic subduction zone, where the African plate is subducted northward beneath Eurasia (Papanikolaou, 1987; Wortel et al., 1993; Ring et al., 2003). In the Cycladic area, three main units can be distinguished, separated by tectonic contacts: (1) the para-autochtonous Basement Unit consisting of

metasediments and orthogneisses, (2) the Cycladic Blueschist Unit (CBU) composed of metasediments and metabasites, and (3) the Upper Unit made up of ophiolitic rocks, sediments and pre-Eocene metamorphic rocks (Bonneau, 1984; Robertson and Dixon, 1984). Two main metamorphic events affected the Cycladic area (Ring et al., 2010; Jolivet and Brun, 2010 and references therein): An Eocene blueschist- and eclogite-facies metamorphic event related to burial, stacking and exhumation of the CBU and Basement below the Upper Unit; and a younger Oligo-Miocene greenschist-facies event during crustal extension in the back-arc of the Hellenic subduction zone due to the slab-rollback of the African plate. On several Cycladic islands, Oligo-Miocene extension formed low-angle detachment faults exhuming the CBU from below the Upper Unit.

On Syros, both the CBU and the Upper Unit occur (Keiter et al. 2011 and references therein, Fig.2). The exposed rocks belonging to the CBU are mainly metagabbros, metabasites, metasediments and schists. The overlying Upper Unit, locally named the Vari Unit, consists of orthogneiss and mylonitic schists, and is considered to be juxtaposed by a brittle detachment fault during late Miocene (Ring et al. 2003). New findings however show that the structure of SE Syros is more complex. Detailed mapping by Soukis and Stockli (2013) showed that a third unit composed of chloritic schists, serpentinites and metabasites occurs in a tectonic position between the underlying CBU and the overlying Vari Unit, again juxtaposed by a detachment. Numerous petrological studies constrain the pressure-temperature evolution of the metamorphic rocks (e.g. Trotet et al., 2001b; Schumacher et al., 2008; Philippon et al., 2012), focusing mainly on the blueschist- and eclogite-facies conditions. The only data for the lower-greenschist-facies metamorphism were reported by Trotet et al. (2001b), suggesting active T-P conditions of 300-350 ℃ at 2 kb ar. In this temperature range, the pressure proposed by other authors in more speculative P-T paths is

129 approximately 4 kbar (Keiter et al., 2004; Schumacher et al., 2008, Fig.3). In general
130 an increase in greenschist-facies overprinting toward the SW Syros involves a NE-
131 SW to E-W stretching lineation with a top-to-the-NE and –E sense of shear (Trotet et
132 al., 2001a; Keiter et al., 2004; Philippon et al., 2011).

133 **3. Material and Methods**

134 **3.1 Outcrop description**

135 The investigated outcrop is located N of Delfini in the western part of Syros island at
136 the base of a several tens of meters marble layer in the CBU (Fig.2, UTM35 414840N
137 313839E, the reader is invited to download a high-resolution 3D-model of the outcrop
138 mapped with an unmanned aerial vehicle, from the electronic supplement). The
139 marble is composed of nearly pure, coarse grained calcite. Minor amounts of white
140 mica are dispersed between the calcite grains and, more rarely, concentrated in thin
141 layers. Slight differences in colour and dolomite content reflect the main foliation
142 (average orientation: 015/38, Fig.4a, b). A lineation is defined by the shape preferred
143 orientation of calcite and white mica (Fig.4b, average orientation: 090/11). Shear
144 zones and flanking structures indicate top-to-the-E shear consistent with the
145 observations of Trotet et al. (2001a) in this area of Syros.

146 We focused our study on one large flanking structure (Fig.4a) that is dominated by
147 one central CE characterized by a darker colour and a smaller grain size than the
148 host rock marble and orientated 005/50. The CE is 5 m long and its width varies from
149 1 to 2.5 cm. The angle between the CE and the marble is around 20°. In the vicinity
150 of the CE, the mylonitic foliation of the host rock records a reverse drag in both, the
151 hanging wall and the footwall of the structure and is offset by a top-to-the W shear
152 sense resulting in an angle of around 45° between ma rble foliation and CE right next

153 to the structure. The trace of the schistosity has an inflection point at the immediate
154 margin of the CE (Fig.4d) indicating a change from reverse to normal drag close to
155 the widening CE (Exner and Grasemann, 2011). The displacement along the CE
156 varies from around 20 cm at the lower tip up to 120 cm at the center of the structure
157 (Fig.4c).

158 The orientation of the CE with respect to the background shear direction and the
159 observed drag indicate that the studied flanking structure can be interpreted as an a-
160 type flanking fold (Grasemann and Stüwe, 2001), that formed during top-to-the-E
161 background shearing. Since close to the investigated outcrop, layer-perpendicular
162 fractures are overprinted by ductile shears of various magnitudes, we believe that the
163 studied flanking structured formed along such a crack, which operated as CE, rotated
164 into the shear direction and led to passive folding of the marble host-rock foliation
165 because of the antithetic slip gradient along the CE.

166 Three samples were collected from three different structural locations in and around
167 the flanking structure (Fig.4a, d). Samples 1, 2 and 3 (later separated into 3a and 3b)
168 were collected, respectively, in the host rock at 1.5 m distance from the cross-cutting
169 element, in and around the cross-cutting element in a zone of 60 cm displacement
170 and in and around the cross-cutting element at its location of maximal displacement
171 of 120 cm.

172 Analogue and numerical models, and analytical solutions have shown that flanking
173 structures form at a small background shear strain of $\gamma < 5$ with a rotation rate of the
174 CE similar to a passive marker line (Exner et al., 2004; Kocher and Mancktelow,
175 2005; Reber et al., 2012). Flanking structures are therefore kinematic indicators
176 restricted to low strain. Assuming simple shear deformation, it is possible to calculate
177 the shear strain, for the flanking structure from the geometric relationship between

178 the orientation of a passive marker before and after deformation (Ramsay and Huber,
179 1983):

180 $$\gamma = \cot(\alpha) - \cot(\alpha'), \quad (1)$$

181 where α and α' are respectively the orientation of the passive marker with respect to
182 the simple shear direction before and after deformation. Assuming an initial
183 orientation of the fracture to be perpendicular to the foliation (α = 90°) and
184 considering the orientation of the CE after deformation ($\alpha' \approx$ 20°), the background
185 shear strain that formed the flanking structure was $\gamma <$ 3. This value corresponds to
186 the shear strain recorded by sample 1. Note that γ does not change dramatically,
187 when the flow is not ideal simple shear (further information on the calculation of the
188 overall background-shear strain can be found in the appendix A2).

189 At the position of sample 2, the offset of the marker layers indicates 64 cm
190 displacement along the CE and the CE has a thickness of 1.2 cm. Assuming simple
191 shear the shear strain is $\gamma =$ 53. Sample 3 comes from the centre of the CE where
192 the displacement is at its maximum of 120 cm and the CE is 1.5 cm thick. Assuming
193 homogeneous simple shear, the values correspond to a shear strain $\gamma =$ 80. At this
194 locality, two very fine-grained, porcelain-like layers flank the CE. If we assume that
195 these fine-grained layers with a total thickness of 0.12-0.48 cm, accommodated most
196 of the displacement, the shear strain is in the range of 250 < $\gamma <$ 1000. Because of
197 the macroscopic heterogeneous appearance, sample 3 was further split for analysis
198 into coarser grained sample 3a and a sample 3b comprising the fine-grained-
199 localized zones. Based on our microtectonic studies we separate three strain
200 domains: low-strain domain (sample 1 and 3a), intermediate-strain domain (sample
201 2) and high-strain domain (sample 3b). Finally, assuming that the microstructures in

the three strain domains formed simultaneously, the three shear-strain domains also reflect strain-rate domains. Consequently, when the flanking structure formed, the strain rate in the CE was up to three orders of magnitude greater than in the host rock. Given the model for flanking structures, the strain rate at a given point can be assumed as constant, and therefore, this well-preserved structure can be regarded as a result of a progressive ductile deformation.

3.2 Sample preparation

The samples were cut in the inferred local XZ plane of finite strain. Sample 1 was cut perpendicular to the main foliation and parallel to the stretching lineation. Samples 2, 3a and 3b were cut perpendicular to the CE boundary and parallel to the stretching lineation of the CE. It must therefore be emphasized that the sample reference frames are different. They are all cut along an approximately vertical plane striking E-W but differ by an up to 45° rotation around a hori zontal N-S axis.

Mechanically polished thin-sections with a thickness of about 20 to 30 µm were prepared for microstructure analysis. Thin sections selected for scanning electron microscopy and electron backscatter diffraction analysis (EBSD) were additionally chemomechanically polished with an alkaline colloidal silica suspension (Köstrosol 3530; pH 9.2-10). These samples were coated with a thin carbon film to establish electric conductivity.

3.3 Microstructure analysis

Microstructure and modal composition of the samples were analysed with a Leica DM4500 P optical microscope. Optical micrographs were taken with plane and crossed polarized light (Fig.5, 6).

Digitized optical micrographs and EBSD data were used for grain shape analysis. The grain parameters were automatically measured by using the DiAna V3 software (© J. Duyster). The 2D-orientation of the grain long axes are presented in rose diagrams to show shape preferred orientation (SPO) within the fabric (Fig.5, insets). The orientations are given in degrees, anticlockwise with respect to the reference frame. The grain size is characterized by the equivalent diameter *d* that is calculated as follows:

$$d = 2\sqrt{A/\pi}, \qquad \text{Eq. 2}$$

where *A* is the grain area. For the different samples and microstructural areas, the distribution of grain size is represented in histograms and the mean grain sizes and standard deviation are reported (Fig.7).

3.4 Texture analysis

Crystallographic preferred orientations (CPOs), grain-shape parameters and the grade of intracrystalline deformation in terms of misorientation were measured by combined EBSD mapping and EDX-spectrometry on a FEI Quanta 3D FEG instrument. The FIB-SEM is equipped with a field-emission electron source and an EDAX Pegasus Apex 4 system consisting of a Digiview IV EBSD camera and an Apollo XV silicon drift detector for EDX-spectrometry. The instrument was operated with a 10 or 15 kV accelerating voltage, a 4 nA probe current and at working distances ranging between 10 and 14 mm and a sample tilt angle of 70°. Different calcite microfabric areas were mapped by beam scanning in square or hexagonal grid mode using a fixed step size in a range between 0.25 and 3.7 µm specifically chosen depending on the grain size. During data collection, the EBSD camera was set to an exposure time of 47 - 103 ms using a camera binning of 4x4 (348x260 pixel)

or 8x8 (174x130 pixel). The Hough space resolution was set to a binned pattern size of 140-160 and a Theta step size of 1°. A Rho fraction of 80-85 % was used for band detection and indexing in order to exclude weak marginal portions of the EBSD pattern. For all data, a 9x9 convolution mask was applied to determine 6-10 or 6-12 peaks at a minimum peak distance of 10-15 pixels in Hough space. With the given settings, indexing rates of 10-21 points per second were achieved.

The OIM Data Collection and Analysis software were used for indexing and processing the EBSD data. Indexing of Kikuchi patterns was based on EDX intensity ranges for specific elements to identify the phases by composition. Grain boundaries were set at a misorientation angle greater than 15° between adjacent points. For detailed texture analysis, host grains and recrystallized grains were separated according to their size and shape. Orientation distribution functions (ODFs) were calculated after Bunge (1982). The orientation of the c (0001), -a <11-20>, a <-1-120> axes and r planes {10-14} were derived from the ODF by use of the MATLAB toolbox for quantitative texture analysis MTEX (https://code.google.com/p/mtex, Bachmann et al., 2010). The data are plotted as equal area upper hemisphere projections (Fig.8).

The misorientation-angle distributions of neighbouring grains (correlated) and for every grain related to every other grain, belonging to one grain population (uncorrelated, see for example Halfpenny et al, 2012), was detected by the OIM Data Analysis software and are represented together with the calculated theoretical, random misorientation-distribution curve for trigonal crystal symmetry (Fig.9, Mackenzie and Thomson, 1957).

4. Results

Microfabrics for the different strain domains are described in terms of grain size distribution, SPO, texture and misorientation-angle distribution. Using the terminology of Sibson (1977) the marble microstructures are distinguished based on the fraction of recrystallized grains:

protomylonites, mylonites and ultramylonites have less than 50% fractions, 50% to 90% fractions and more than 90% fractions recrystallized grains, respectively. Additionally, fine grained ultramylonites are ultramylonites having an average grain size less than 9 μm.

4.1 Marble microfabric in the low-strain domain

The microstructure of the low-strain domain marble is characterized by coarse calcite grains with a grain size around 300 μm (Fig.5a, b). Within dolomite-rich layers (dolomite fraction larger than 20%), calcite grains are smaller with grain sizes ranging between 25 and 245 μm. The grain-size-distribution plot shows two peaks, one well defined at 150 μm and a second less pronounced at 300 μm (Fig.7a). The grains show a strong SPO with the long axes oriented at 40°, consistent with the top-to-the E sense of shear in the host rock. Undulatory extinction and the minor presence of subgrain boundaries indicate intracrystalline deformation. Grain boundaries are slightly curved showing evidence of grain boundary migration (GBM). Conjugate narrow or tabular twins are observed corresponding to Type I and Type II twins respectively (Ferrill et al., 2004).

The texture of the low strain domain is mainly characterized by a strong maximum of c axis perpendicular to the foliation (Fig.8a). There is only a weak girdle arrangement of a and -a axes approximately 50 ° inclined to the f oliation plane while the r planes

do not record a preferred orientation. The observed clusters represent single crystal maxima.

Next to the CE (sample 3a), similar microstructural and textural features are rotated by an angle of 40° to 50°, consistent with the passive rotation of the main foliation due to the reverse drag close to the CE (Fig.8b). As a result, the long axes of the grains are parallel to the CE boundary (Fig.5b). Misorientation distribution curves for correlated and uncorrelated grains differ radically from the random misorientation distribution. They have a common peak located between 45 and 60° (Fig.9a). An additional peak occurs at 80° for the correlated grains and at 30° for uncorrelated grains.

4.2 Marble microfabric in the intermediate-strain domain

The microstructure of the intermediate-strain domain is characterized by a strong foliation (CE plane) defined by alternating protomylonitic and ultramylonitic layers (Fig.5c, d, g, h). Thickness measurements in thin sections, reached values up to 4 mm for protomylonitic and up to 800 µm for ultramylonitic layers.

Within protomylonite layers, the calcite grains are elongate and show strong intracrystalline deformation (Fig.5d, g). Undulatory extinction and curved twins are common. Locally, sutured twin- and grain-boundaries can be observed. Larger calcite porphyroclasts (average grain size 52 µm, Fig.7b) built-up of subgrains (average grain size 13 µm, Fig.7c) are surrounded by recrystallized grains with a similar size as the subgrains (average grain size of 9.5 µm, Fig.7d), creating a core-mantle structure. The recrystallized grains have a SPO oriented at 150° consistent with the antithetic top-to-the-W sense of shear in the CE (Fig.5d). The ultramylonitic layers consist of equigranular calcite (Fig.5c, h). The grain size ranges between 5 µm and

40 µm, with an average of 10 µm (Fig.7e). The grains show a strong SPO aligned at an angle of around 120° to 150° relative to the CE b oundary defining a secondary foliation (Fig.5c, h). Notice that the recrystallized grains from the protomylonitic and ultramylonitic layers have similar grain size and SPO characteristics.

White mica grains within the protomylonitic layers lie parallel to the cross-cutting element boundary consistent with the stretching direction of the calcite grains (Fig.6a). Micas within the ultramylonitic layers are aligned with their long axes parallel to the long axes of recrystallized calcite grains (Fig.6b). Quartz is present as single grains lacking any evidence for a preferred orientation or intracrystalline deformation like undulatory extinction, bulging or subgrain formation and are therefore essentially behaving as rigid clasts.

The deformed calcite host grains show a strong point maximum of c axis inclined 30 to 40° to the z-axis of the pole figure while the a and –a axes show three maxima aligned on a girdle normal to the c axis (Fig.8c). The separated a and –a axes pole figures can be transformed into each other by a rotation of 180° around the crystal c axis. The texture contains a two-fold-symmetry axis parallel to y axis of the sample and records therefor a monoclinic symmetry.

The c axis of recrystallized grains from core-mantle structures within the protomylonitic layers and c axis of grains within the ultramylonitic layers are normal to the CE plane while the a and –a axes form a girdle in the CE plane (Fig.8d, e). There is no clear difference of a and –a axis distribution noticeable for the grains in the ultramylonitic layers. The texture corresponds therefore approximately to an orthorhombic symmetry with three two-fold-symmetry axes parallel to the sample z, y, and x axis respectively. The main maximum of the r poles is orientated slightly oblique to the pole of the CE plane.

Host grains, recrystallized grains of protomylonitic layers and grains of ultramylonitic layers within the intermediate strain zone show a clear CPO although an increasing amount of recrystallized grains is associated with a slight decrease in CPO strength (Fig.8c , d, e). Disregarding differences in the intensity of the distribution, the texture of recrystallized grains is apparently the result of an anticlockwise rotation of the texture of the host grains around the sample y axis.

In the core-mantle structure, both misorientation-angle-distribution curves for correlated and uncorrelated grains differ from the random misorientation-angle distribution. Similar to the low-strain domain the curve for uncorrelated grains shows a peak at around 50° while the misorientation-angle-distribution curve for correlated grains shows a peak at 80° and higher frequencies at misorientation angles smaller 20° (Fig.9b).

For the ultramylonitic layer, both curves also differ from the random one. The curve for uncorrelated grains is approximately the same as for the protomylonite but with a less distinct peak around 50 to 60° (Fig.9d). Except for a small gain at low misorientation angles and slightly smaller frequencies at greater misorientation angles, the curve for correlated grains is similar to the curve for uncorrelated grains.

4.3 Marble microfabric in the high-strain domain

The microstructure of the high-strain domain is characterized by protomylonitic, ultramylonitic and fine-grained ultramylonitic layers. Fine grained ultramylonitic layers occur only close to the boundary between the cross-cutting element and the host rock. Thickness measurements in thin section reached values up to 1750 µm for protomylonitic, up to 1500 µm for ultramylonitic and up to 240 µm for fine-grained ultramylonitic layers.

In protomylonitic layers, core-mantle structures compare well to the intermediate-strain domain. They show intensely deformed calcite grains (average grain size 68 µm, Fig.7f) that partly contain wedge shaped twins preferentially oriented with an angle of 150° with respect to the cross-cutting element boundary. The larger calcite grains contain a high amount of subgrains with an average grain size of 11.5 µm (Fig.7g) and are surrounded by recrystallized with a similar average grain size (10.5 µm, Fig.7h).

Recrystallized grains of ultramylonitic layers have an average grain size of 13 µm (Fig.7i). Their long axes are aligned between 110° and 150°, the SPO is more pronounced than in the other domains (Fig.5e). Close at the boundary to the fine grained ultramylonite, a higher amount of small bulges can be observed at boundaries of ultramylonitic grains (Fig.5k).

Fine-grained ultramylonitic layers have an average grain size of 3.3 µm (Fig.7j). The grains show a weaker SPO than those in the ultramylonite (Fig.5f). Locally triple-junctions with nearly dihedral 120° angles occur (Fig.5 k, l).

Within the protomylonitic layers, the calcite texture of host grains and surrounding recrystallized grains are similar (Fig.8f, g). The c axis of host grains are oriented perpendicular to the CE plane, whereas three separated point maxima of a axes are aligned on a girdle within the CE plane. The recrystallized grains of the core-mantle structure show approximately the same CPO although less pronounced.

The texture of the new recrystallized grains from the ultramylonitic layers differs significantly from that of the intermediate-strain domain (Fig.8h). The c axes of calcite grains in the ultramylonitic layers form a girdle normal to the lineation while the a and

–a axes form point-maxima parallel to the lineation. The r poles are aligned in a crossed girdle.

The texture of grains from the fine-grained ultramylonitic layers is weak with a texture index of 1.4. It differs from the texture of ultramylonitic grains by a 90° rotation around the sample z axis, leading to a point-maximum of a and –a axes in the centre of the pole figure and c axis arranged at the periphery of the pole figure (Fig.8i).

The distribution curve for misorientation angles of the protomylonite lack the peak at around 50 to 60° for uncorrelated grains reflected by all other microstructures so far. Instead, a local minimum around 40 to 50° can be observed for correlated and uncorrelated grains. Both curves show a peak around 80° characteristic for e-twinning in calcite (Fig.9c). The misorientation-angle distribution for uncorrelated ultramylonitic grains is bell-shaped with a maximum around 60°. The curve for correlated grains shows a strong peak at 80° (Fig.9e). In fine-grained ultramylonitic layers the misorientation curves for correlated and uncorrelated grains are very close to the theoretical curve for random grains (Fig.9f).

5. Discussion

5.1 Relative timing of microstructure development

The observed microstructures can be linked to the two different metamorphic events that affected Syros. On the one hand, within the low strain domain, the observed coarse calcite grains are likely the result of grain growth at elevated temperatures (Barnhoorn et al., 2004) during the blueschist or eclogite facies evolution of Syros metamorphic rocks (at 400-550 ℃). Smaller grain sizes in this strain domain, are always correlated to the presence of greater amounts of dolomite grains. Therefore,

415 we assume that the presence of the second phase inhibits grain growth, causing a
416 smaller calcite grain size (Olgaard and Evans, 1986, 1988; Tullis and Yund, 1982).

417 On the other hand, features related to ductile deformation within all three strain
418 domains like curved grain boundaries, undulatory extinction, development of core-
419 mantle structures and mylonitization are likely to be related to Miocene-greenschist-
420 facies deformation. If these structures had formed during early blueschist-eclogite-
421 facies metamorphism, they would have been annealed, producing straight grain
422 boundaries and absence of undulatory extinction. A second source of evidence for
423 development during greenschist-facies metamorphism is that experimental study of
424 calcite annealing shows a switch in the r axes alignment, producing a preferential
425 orientation of one r pole maxima in the shear plane and another one normal to the
426 shear direction if annealing occurs (Barnhoorn et al., 2005). Such a texture is absent,
427 so we infer that the crystallographic texture of these structures was not annealed,
428 and postdated the earlier metamorphism. Another factor supporting deformation
429 during greenschist-facies metamorphism is that the orientation of the recrystallized
430 grain long axes within the host rock display top-to-the-east sense of shear observed
431 on Syros during the later metamorphism (Keiter et al., 2004).The orientation deviation
432 of the SPO as well as the CPO of the grains next to the CE is apparently caused by
433 the passive rotation of the host rock foliation during flanking structure development
434 (Grasemann et al., 2005). The observed angle of 40° to 50° is identical to th e
435 structural field measurements, texture and SPO indicating that the observed SPO
436 and CPO preceded flanking-structure formation.

437 **5.2 Strain-rate dependent calcite deformation and recrystallization mechanisms**

438 Within the low-strain domain, the microfabric is characterized by preferentially
439 orientated, coarse-grained calcite marble**.** The strong SPO with grain long axis

orientated at 40° to the foliation can result from to p-to-the-E shearing during crystal plastic-deformation. The observed undulose extinction indicates the presence of geometrical necessary dislocations which may cause the development of a CPO (Hirth and Tullis, 1992). Although dissolution precipitation creep and stress-directed grain growth may also lead to the formation of a weak CPO (Bons and den Brok, 2000), these processes are not considered to be responsible for the observed SPO because crystal-plastic deformation can be directly linked with undulose extinction and presence of subgrains. Slightly curved grain boundaries are probably the result of grain-boundary migration (GBM) indicating that the deformation took place within the dislocation-creep regime. Temperatures above 200 ℃, which have most likely prevailed in the investigated rocks, already activate dynamic recrystallization in calcite (Herwegh and Pfiffner, 2005), which is therefore likely to deform by GBM at moderate temperatures as observed by Spacek et al. (2001) and Kennedy and White (2001).

With increasing strain and strain rate, deformation results in further intracrystalline deformation of the grains and formation of small recrystallized grains along the boundaries of pre-existing grains. These protomylonitic zones are characterized by a core-mantle structure where host grains are surrounded by recrystallized grains. The fact that subgrains within the host grains and recrystallized grains show almost the same size indicates that SGR was the dominant recrystallization mechanism. Similar core-mantle structures occur already at low shear strains in naturally deformed calcite (Bestmann et al., 2000) and experimentally at shear strains between $2 < \gamma < 5$ (Schmid et al., 1987).

The surrounding recrystallized grains show a reorientation of the c axis perpendicular to the foliation whereas the a and -a axes form a girdle within the foliation plane. The

strong difference in misorientation angle distribution curves for correlated and uncorrelated grains indicates a dependence of neighbouring grains, emphasizing that SGR was the dominant deformation mechanism (Bestmann et al. 2000; Wheeler et al., 2001). With progressive deformation, further recrystallization occurs resulting in the formation of ultramylonitic layers with more than 90 % recrystallized grains. Due to grain-boundary alignment of the new recrystallized grains, a secondary foliation oblique to the CE-boundary develops (Barnhoorn et al., 2004). The change in texture symmetry from monoclinic to orthorhombic is most likely caused by activation of a different slip system.

Deformation at greater strain and strain rate results in similar microstructures as within the intermediate strain domain such as core-mantle structures and the development of ultramylonitic layers. Also in the high-strain domain, subgrains of host grains and surrounding recrystallized grains show a similar grain size, indicating that SGR was the dominant recrystallization mechanism implying that dislocation creep was active.

The greater amount of wedge-shaped deformation twins, within the host grains in the high-strain domain is accompanied by an increased frequency at 80° for misorientation angles of correlated grains (Bestmann et al., 2000; Burkhard, 1993).

The microstructure of the fine grained ultramylonite is characterized by (1) an extremely small grain size, (2) grain boundary triple junctions with nearly 120° angles (Fig. 5k,l), (3) a weak CPO with very low texture index (J = 1.4) and (4) a random misorientation distribution curve. The preferential location of small grains next to the ultramylonitic layer (average 13 µm) showing a greater amount of small bulges, indicates that the fine-grained ultramylonite developed at the expense of the ultramylonite. These observations can result from two different deformation

behaviours for the development of the fine-grained ultramylonitic layers. The fine grain size could result from brittle grain-size reduction followed by cataclastic flow, leading to the randomization of the misorientation distribution. Subsequent annealing of the microstructure could result in the development of a weak CPO. The second behaviour would be grain-size reduction by bulging (BLG) recrystallization during dislocation creep, followed by a grain-size sensitive (GSS) deformation mechanism, such as grain-boundary sliding (GBS). Again, a random misorientation distribution would be generated and at the same time, minor dislocation creep would have produced the observed weak CPO. Since we do not see any positive evidence for brittle deformation in the microstructure, but small bulges at grain boundaries of ultramylonitic grains, we assume BLG recrystallization to be the more likely mechanism. The greater strain-rate at the location of maximal displacement may have caused the switch from SGR to BLG at the same metamorphic conditions.

The dependence of the dynamic recrystallization mechanism on strain rate and temperature is well described for quartz (Hirth and Tullis, 1992; Stipp et al. 2002; Stipp and Kunze, 2008). Especially, GBM, SGR and BLG are activated in quartz aggregates with increasing strain rate and decreasing temperature (Stipp et al., 2002). For calcite such a clear characterization is missing. Nevertheless an increase in GBM activity occurs with increasing temperature and increasing strain (Schmid et al., 1987, Barnhoorn et al., 2004). The occurrence of SGR and BLG seems to be more simultaneously although BLG is less common in calcite (Pieri et al., 2001; Barnhoorn et al., 2004). Here, we can directly link the activation of BLG recrystallization to an increase in strain rate.

We infer that the fine grain size and random misorientation distribution curve for fine-grained ultramylonitic layers means that the dominant deformation mechanism was

515 GSS flow where grain-boundary sliding (GBS) was active and probably
516 accommodated most of the strain (Schmid et al., 1987; Fliervoet, 1997; Bestmann
517 and Prior, 2003). Nevertheless, GBS behaviour necessitates at least one more
518 deformation mechanism to avoid overlaps between blocking grains and the formation
519 of voids. In this particular case, we infer that the observed weak CPO indicates that
520 minor dislocation creep was active with GBS.

521 The deformation behaviour of calcite at greater strain rates is comparable with the
522 one at intermediate strain rates. SGR recrystallization seems to be the most common
523 recrystallization mechanism over a wide strain rate range resulting in the formation of
524 ultramylonitic layers. Nevertheless, different gliding systems can be activated with
525 increasing strain rates leading to the formation of a different texture (Fig.8).
526 Additionally, BLG recrystallization became more prevalent at greater strain rates,
527 resulting in a smaller grain size for which GSS mechanisms are activated. The main
528 observations from microstructures, textures, deformation- and recrystallization
529 mechanism are illustrated in Figure 10. The microfabrics are linked to estimated
530 strain and strain rates with the potential to act as a reference and standard for natural
531 systems and also, serving as a comparison for experimental deformation results.

532 **5.3 Comparison with experimental calibrations**

533 A differential stress-grain size deformation-mechanism map for marble has been
534 calculated using grain-size insensitive (GSI) calcite flow laws for dislocation creep
535 (Renner et al., 2002) and GSS creep (Herwegh et al., 2003), which represents a
536 combination of diffusion creep and GBS (see appendix A1). Based on the observed
537 microfabrics and the top-to-the-East shear associated with the second metamorphic
538 event on Syros, a deformation temperature corresponding with lower greenschist-
539 facies conditions is used (300 ℃). The boundary between the GSS and the GSI field,

which can be considered to correspond to stabilization of the grain size at values balancing GSS and GSI creep (De Bresser et al., 1998, 2001) was calculated and added to the map. Additionally, the paleowattmeter for calcite (Austin and Evans, 2009) and the paleopiezometers (Schmid, 1980; Rutter, 1995) linking stable grain size and differential stress are plotted (Fig.11). Further information on used calibrations is given in the appendix.

The differential stress and strain rate conditions of the different microstructures are determined by assuming that the average grain size of the fine grained ultramylonite represents a stable grain size. At a grain size of about 3 µm, both paleowattmeter and field boundary are consistently indicating a differential stress of 200 MPa. Differential stress conditions suggested by the paleopiezometer of Schmid (1980) are slightly less at around 170 MPa. The differential stress conditions corresponding to the remaining microfabrics are determined using the strain-rate ratios and the grain sizes of the microstructures observed within the different strain domains. For the stable grain size of the intermediate-strain domain (10 µm), the calculated differential stress conditions vary significantly depending on the chosen paleo-piezometer/-wattmeter. The field boundary and the paleopiezometer of Schmid (1980) are consistent with our results, indicating a differential stress of around 45 MPa while the paleowatmeter and the paleopiezometer by Rutter (1995) for SGR suggest greater values of around 75 MPa and 150 MPa, respectively. Differential stresses for the low -strain domain calculated by the paleopiezometer of Rutter (1995) for GBM agree with our values of around 25 MPa.

Consistent with our microstructural observations, deformation starts within the dislocation creep field (Fig.11, GSI) in all three strain domains. Progressive deformation at constant strain rates, decreases grain size, shifting the resulting grain

size range closer to the field boundary. Decreasing grain size induces increasing viscosity at about $10^{0.5}$ Pa s, within the high- and intermediate-strain domains. This changing viscosity for constant strain rates indicates minor strain hardening during the dislocation creep. This evolution is consistent with the observed change from reverse to normal drag next to the CE, where the CE would have been widening during rotation and slip (Means, 1995; Pennacchioni and Mancktelow, 2007). Within the high-strain domain, the grain size decreases even further so that a GSS deformation mechanism is activated. The switch in deformation regime leads to strain softening as indicated decreasing viscosity with increasing strain rate. This softening evolution is consistent with extreme localization of the deformation in the fine-grained ultramylonite (Bestmann et al., 2000).

In the ultramylonite, calculated shear-strain rate values are between $10^{-9.5}$ s^{-1} and 10^{-10} s^{-1}. The calculated strain rate for the background shear, leading to the rotation of the cross-cutting element is around $10^{-12.5}$ s^{-1}, which lies at the higher bound of typical strain rates in shear zones at crustal levels (Pfiffner and Ramsay, 1982).

These predictions about deformation strain rates and differential stresses are in agreement with a deformation temperature of 300 ℃. Deformation at higher temperatures would result in an unexpectedly high background shear-strain rate of around 10^{-11} s^{-1}, a value which is too great considering the small amount of intracrystalline deformation. Lower deformation temperatures would favour deformation in the ductile-brittle transition zone which we do not believe occurred given the preserved microstructures in the study area.

Our observations show that the field boundary theory as well as the calcite paleowattmeter (Austin and Evans, 2009) and the paleopiezometer of Schmid (1980) can be extrapolated to natural examples deformed at strain rates > 10^{-12} s^{-1}. At lesser

strain rates, the paleowattmeter seems to underestimate conditions. In contrast the paleopiezometer of Rutter (1995) for SGR seems to result in slightly overestimated values while the one for GBM is consistent with our observations.

6. Conclusions

We used a flanking structure as a natural laboratory for studying the microfabric and effective deformation mechanisms of nearly pure calcite marble for lower greenschist facies conditions (~300 ℃) and different strain rates (10^{-12} to 10^{-9} s^{-1}). Natural strain-rates and grain sizes were compared with experimentally determined flow laws, paleowatt- and paleopiezo-meters, resulting to the following conclusions.

(1) The recrystallization mechanism of calcite changed with increasing strain rate from grain-boundary migration (GBM) to subgrain rotation (SGR) and finally bulging (BLG) recrystallization. SGR seems to be, however, the dominant recrystallization mechanism over a wide range of strain rates. The switch in recrystallization mechanism is accompanied by a decrease in grain size.

(2) Strain progressively localizes along fine-grained layers. Ultramylonitic layers evolve from mature core-mantle structures by SGR while fine-grained ultramylonitic layers developed from ultramylonitic layers by BLG recrystallization.

(3) The change of calcite textures indicate that activation of different gliding systems depends on different strain rates.

(4) Laboratory-determined flow laws for GSI creep (Renner et al., 2002) and GSS creep (Herwegh et al., 2003) are consistent with our observations regarding the activity of different creep regimes and the predictions for the evolution of hardening and softening at constant strain rates.

(5) Paleostress calculated with the paleowattmeter of Austin and Evans (2009) and the paleopiezometer of Schmid (1980) give reliable results for calcite deformed at strain rates faster 10^{-12} s^{-1}. In contrast, the paleopiezometer of Rutter (1995) for SGR recrystallization seems to predict overestimated values.

(6) The results of this study are only valid for the lower greenschist facies and high strain rates (10^{-12} to 10^{-9} s^{-1}). More work using well constrained natural high-strain calcite rocks at higher grade is needed to extend the validity of experimental calibrations at natural strain rates.

Acknowledgment

We thank the University of Vienna (grant number IK543002) for supporting the doctoral school DOGMA ("Deformation of geological materials") and the Austrian Science Foundation FWF for funding the project "Mineral reactions and deformation in host-inclusion settings" (grant number I471-N19) as part of the international research group FOR741-DACH. Valuable discussions with Hugh Rice, Claudia Trepmann, Michel Bestmann and Dave Schneider are greatly appreciated. Detailed and insightful comments by the reviewers Joerg Renner and Michael Stipp are gratefully appreciated. We would also like to thank William M Dunne for editorial handling.

References

Austin, N., Evans, B., Herwegh, M., Ebert, A., 2008. Strain localization in the Morcles nappe (Helvetic Alps, Switzerland). Swiss Journal of Geosciences 101, 341-360.

635 Austin, N., Evans, B., 2009. The kinetics of microstructural evolution during
636 deformation of calcite. Journal of Geophysical Research 114, B09402,
637 doi:10.1029/2008JB006138.
638
639 Bachmann, F., Hielscher, R., Schaeben, H., 2010. Texture Analysis with MTEX –
640 Free and Open Source Software Toolbox. Solid State Phenomena 160, 63-68.
641
642 Barber, D.J., Wenk, H.R., Gomez-Barreiro, J., Rybacki, E., Dresen, G., 2007. Basal
643 slip and texture development in calcite: new results from torsion experiments.
644 Physics and Chemistry of Minerals 34, 73-84.
645
646 Barnhoorn, A., Bystricky, M., Burlini, L., Kunze, K., 2004. The role of recrystallisation
647 on the deformation behaviour of calcite rocks: large strain torsion experiments on
648 Carrara marble. Journal of Structural Geology 26, 885-903.
649
650 Barnhoorn, A., Bystricky, M., Burlini, L., Kunze, K., 2005. Post-deformational
651 annealing of calcite rocks. Tectonophysics 403, 167-191.
652
653 Bestmann, M., Kunze, K., Matthews, A., 2000. Evolution of a calcite marble shear
654 zone complex on Thassos Island, Greece: microstructural and textural fabrics and
655 their kinematic significance. Journal of Structural Geology 22, 1789-1807.
656 Bestmann, M., Prior, D. J., 2003. Intragranular dynamic recrystallization in naturally
657 deformed calcite marble: diffusion accomodated grain boundary sliding as a result of
658 subgrain rotation recrystallization. Journal of Structural Geology 25, 1597-1613.
659

660 Bestmann, M., Prior, D.J., Grasemann, B., 2006. Characterisation of deformation and
661 flow mechanics around porphyroclasts in a calcite marble ultramylonite by means of
662 EBSD analysis. Tectonophysics 413, 185-200.
663
664 Bobyarchick, A.R., 1986. The eigenvalues of steady flow in Mohr space.
665 Tectonophysics 122, 35-51.
666
667 Bons, P.D., den Brok, B., 2000. Crystallographic preferred orientation development
668 by dissolution--precipitation creep. Journal of Structural Geology 22, 1713-1722.
669
670 Bonneau, M., 1984. Correlation of the Hellenide nappes in the south-east Aegean
671 and their tectonic reconstruction. Geological Society, London. Special Publications
672 17, 517-527.
673
674 Bunge, H. J., 1982. Texture Analysis in Materials Science: Mathematical Models.
675 Butterworths, London.
676
677 Burkhard, M., 1993. Calcite twins, their geometry, appearance and significance as
678 stress-strain markers and indicators of tectonic regime: a review. Journal of Structural
679 Geology 15, 351-368.
680
681 De Bresser, J.H.P., Spiers, C.J., 1997. Strength characteristics of the r, f, and c slip
682 systems in calcite. Tectonophysics 272, 1-23.
683

684 De Bresser, J. H. P., Peach, C., Reijs, J., Spiers, C., 1998. On dynamic
685 recrystallization during solid state flow: Effects of stress and temperature.
686 Geophysical Research Letters 25, 3457-3460.
687
688 De Bresser, J. H. P., Ter Heege, J., Spiers, C., 2001. Grain size reduction by
689 dynamic recrystallization: Can it result in major rheological weakening? International
690 Journal of Earth Sciences 90, 28-45.
691
692 De Bresser, J. H. P., Evans, B., Renner, J., 2002. On estimating the strength of
693 calcite rocks under natural conditions. Deformation Mechanisms, Rheology and
694 Tectonics: Current Status and Future Perspectives, Geological Society, London.
695 Special Publications 200, 309-329.
696
697 De Paor, D.G., Means, W.D., 1984. Mohr circles of the First and Second Kind and
698 their use to represent tensor operations. Journal of Structural Geology 6, 693-701.
699
700 Exner, U., Mancktelow, N.S., Grasemann, B., 2004. Progressive development of s-
701 type flanking folds in simple shear. Journal of Structural Geology 26, 2191-2201.
702
703 Exner, U., Grasemann, B., 2010. Deformation bands in gravels: displacement
704 gradients and heterogeneous strain. Journal of the Geological Society 167, 905-913.
705
706 Ferrill, D. A., Morris, A. P., Evans, M. A., Burkhard, M., Groshong, R. H., Onasch, C.
707 M., 2004. Calcite twin morphology: a low-temperature deformation geothermometer.
708 Journal of Structural Geology 26, 1521-1529.
709

710 Fliervoet, T. F., White, S. H., Drury, M. R., 1997. Evidence for dominant grain-
711 boundary sliding deformation in greenschist- and amphibolite-grade polymineralic
712 ultramylonites from the Redbank Deformed Zone, Central Australia. Journal of
713 Structural Geology 19, 1495-1520.
714
715 Grasemann, B., Stüwe, K., 2001. The development of flanking folds during simple
716 shear and their use as kinematic indicators. Journal of Structural Geology 23, 715-
717 724.
718
719 Grasemann, B., Martel, S., Passchier, C., 2005. Reverse and normal drag along a
720 fault. Journal of Structural Geology 27, 999-1010.
721
722 Grasemann, B., Exner, U., Tschegg, C., 2011. Displacement-length scaling of brittle
723 faults in ductile shear. Journal of Structural Geology 33, 1650-1661.
724
725 Halfpenny, A., Prior, D.J., Wheeler, J., 2012. Electron backscatter diffraction analysis
726 to determine the mechanisms that operated during dynamic recrystallisation of
727 quartz-rich rocks. Journal of Structural Geology 36, 2-15.
728
729 Herwegh, M., Xiao, X., Evans, B., 2003. The effect of dissolved magnesium on
730 diffusion creep in calcite. Earth and Planetary Science Letters 212, 457-470.
731 Herwegh, M., Pfiffner, O.A., 2005. Tectono-metamorphic evolution of a nappe stack:
732 A case study of the Swiss Alps. Tectonophysics 404, 55-76.
733
734 Hirth, G., Tullis, J., 1992. Dislocation creep regimes in quartz aggregates. Journal of
735 Structural Geology 14, 145-159.

Jolivet, L., Brun, J.-P., 2010. Cenozoic geodynamic evolution of the Aegean. International Journal of Earth Sciences 99, 109-138.

Keiter, M., Piepjohn, K., Ballhaus, C., Lagos, M., Bode, M., 2004. Structural development of high pressuremetamorphic rocks on Syros island (Cyclades, Greece). Journal of Structural Geology 26, 1433-1445.

Keiter, M., Ballhaus, C., Tomaschek, F., 2011. A new geological map of the Island of Syros (Aegean Sea, Greece): Implications for lithostratigraphy and structural history of the Cycladic Blueschist Unit. The Geological Society of America, Special Paper 481.

Kennedy, L.A., White, J.C., 2001. Low-temperature recrystallization in calcite: Mechanisms and consequences. Geology 29, 1027-1030.

Kocher, T., Mancktelow, N.S., 2005. Dynamic reverse modelling of flanking structures: a source of quantitative kinematic information. Journal of Structural Geology 27, 1346-1354.

Kurz, W., Neubauer, F., Unzog, W., Genser, J., Wang, X., 2000. Microstructural and textural development of calcite marbles during polyphase deformation of Penninic units within the Tauern Window (Eastern Alps). Tectonophysics 316, 327-342.

760 Liteanu, E., Niemeijer, A., Spiers, C.J., Peach, C.J., de Bresser, J.H.P., 2012. The
761 effect of CO2 on creep of wet calcite aggregates. Journal of Geophysical Research
762 117, B03211.
763
764 Llana-Fúnez, S., Rutter, E. H., 2008. Strain localization in direct shear experiments
765 on Solnhofen limestone at high temperature - Effects of transpression. Journal of
766 Structural Geology 30, 1372-1382.
767
768 Mackenzie, J. K., Thompson, M. J., 1957. Some statistics associated with the
769 random disorientation of cubes. Biometrika 44, 205-210.
770
771 Means, W.D., 1995. Shear zones and rock history. Tectonophysics 247, 157-160.
772
773 Oesterling, N., Heilbronner, R., Stunitz, H., Barnhoorn, A., Molli, G., 2007. Strain
774 dependent variation of microstructure and texture in naturally deformed Carrara
775 marble. Journal of Structural Geology 29, 681-696.
776
777 Olgaard, D. L., Evans, B., 1986. Effects of Second-Phase Particles on Grain Growth
778 in Calcite. Journal of the American Ceramic Society 69, C-272-C-277.
779
780 Olgaard, D. L., Evans, B., 1988. Grain growth in synthetic marbles with added mica
781 and water. Contributions to Mineralogy and Petrology 100, 246-260.
782
783 Papanikolaou, D. J., 1987. Tectonic evolution of the Cycladic Blueschist Belt (Aegean
784 Sea, Greece). H.C. Helgeson, Chemical Transport in Metasomatic Processes, 429-
785 450.

786

787 Passchier, C.W., 2001. Flanking structures. Journal of Structural Geology 23, 951-
788 962.

789

790 Pennacchioni, G., Mancktelow, N.S., 2007. Nucleation and initial growth of a shear
791 zone network within compositionally and structurally heterogeneous granitoids under
792 amphibolite facies conditions. Journal of Structural Geology 29, 1757-1780.

793

794 Pfiffner, O. A., Ramsay, J. G., 1982. Constraints on geological strain rates:
795 arguments from finite strain rates of naturally deformed rocks. Journal of Geophysical
796 Research 87, 311-321.

797

798 Philippon, M., Brunn, J. P., Gueydan, F., 2011. Tectonics of the Syros blueschists
799 (Cyclades, Greece): From subduction to Aegean extension. Tectonics 30, TC4001,
800 doi:10.1029/2010TC002810.

801

802 Philippon, M., Brunn, J. P. and Gueydan, F., 2012. Deciphering subduction from
803 exhumation in the segmented Cycladic Blueschist Unit (Central Aegean, Greece).
804 Tectonophysics 524, 116-134.

805

806 Pieri, M., Burlini, L., Kunze, K., Stretton, I., Olgaard, D. L., 2001. Rheological and
807 microstructural evolution of Carrara marble with high shear strain: results from high
808 temperature torsion experiments. Journal of Structural Geology 23, 1393-1413.

809

810 Ramsay, J.G., Huber, M.I., 1983. The Techniques of Modern Structural Geology.
811 Volume 1: Strain Analysis. Academic Press Inc. Ltd, London.

Ratschbacher, L., Wenk, H.R., Sintubin, M., 1991. Calcite textures: examples from nappes with strain-path partitioning. Journal of Structural Geology 13, 369-384.

Reber, J.E., Dabrowski, M., Schmid, D.W., 2012. Sheath fold formation around slip surfaces. Terra Nova 24, 417–421.

Reches, Z., Eidelman, A., 1995. Drag along faults. Tectonophysics 247, 145-156.

Renner, J., Evans, B., Siddiqi, G., 2002. Dislocation Creep of Calcite. Journal of Geophysical Research 107, ECV6-1-ECV6-16.

Ring, U., Thompson, S., Bröcker, M., 2003. Fast extension but little exhumation: the Vari Detachment in the Cyclades, Greece. Geological Magazine 140, 245-252.

Ring, U., Glodny, T., Will, T., Thomson, S., 2010. The Hellenic subduction system: High-pressure metamorphism, exhumation, normal faulting and large-scale extension. Annual Reviews of Earth and Planetary Sciences 38, 45-76.

Robertson, A.H., Dixon, J.E., 1984. Introduction: aspects of the geological evolution of the Eastern Mediterranean, in: Dixon, J.E., Robertson, A.H. (Eds.), The Geological Evolution of the Eastern Mediterranean. Geological Society, London, Special Publications, London, pp. 1-74.

836 Rutter, E.H., 1995. Experimental study of the influence of stress, temperature, strain
837 on the dynamic recrystallization of Carrara marble. Journal of Geophysical Research
838 100, 24651-24663.
839
840 Rybacki, E., Evans, B., Janssen, C., Wirth, R., Dresen, G., 2013. Influence of stress,
841 temperature, and strain on calcite twins constrained by deformation experiments.
842 Tectonophysics 601, 20-36.
843
844 Schmid, S. M., Panozzo, R., Bauer, S., 1987. Simple shear experiments on calcite
845 rocks: rheology and microfabric. Journal of Structural Geology 9, 747-778.
846
847 Schmid, S. M., Paterson, M. S., Boland, J. N., 1980. High temperature flow and
848 dynamic recrystallization in Carrara marble. Tectonophysics 65, 245-280
849
850 Schumacher, J. C., Brady, J. B., Cheney, J. T., Tonnsen, R. R., 2008. Glaucophane-
851 bearing Marbles on Syros, Greece. Journal of Petrology 49, 1667-1686.
852
853 Sibson, R. H. 1977. Fault rocks and fault mechanisms. Geological Society, London
854 133, 191-213.
855
856 Soukis, K., Stöckli, D. F., 2013. Structural and thermochronometric evidence for
857 multi-stage exhumation of southern Syros, Cycladic island, Greece. Tectonophysics
858 595-596, 148-164.
859

860 Spacek, P., Kalvoda, J, Francu, E., Melichar, R., 2001. Variation of deformation
861 mechanisms within the progressive-retrogressive mylonitization cycle of limestones:
862 Brunovistulian Sedimentary Cover (The Variscan Orogeny of the southeastern
863 Bohemian Massif). Geological Carpathica 52, 263-275.
864
865 Stipp, M., Stünitz, H., Heilbronner, R., Schmid, S. M., 2002. The eastern Tonale fault
866 zone: a `natural laboratory` for crystal plastic deformation of quartz over a
867 temperature range from 250 to 700 ℃. Journal of Str uctural Geology 14, 1861-1884.
868
869 Stipp, M., Kunze, K., 2008. Dynamic recrystallization near brittle-plastic transition in
870 naturally and experimentally deformed quartz aggregates. Tectonophysics 448, 77-
871 97.
872
873 Ter Heege, J.H., De Bresser, J.H.P., Spiers, C.J., 2004. Composite flow laws for
874 crystalline materials with log-normally distributed grain size: theory and application to
875 olivine. Journal of Structural Geology 26, 16993-1705.
876
877 Trotet, F., Jolivet, L., Vidal, O., 2001a. Tectono-metamorphic evolution of Syros and
878 Sifnos islands (Cyclades, Greece). Tectonophysics 338, 179-206.
879
880 Trotet, F., Vidal, O., Jolivet, L., 2001b. Exhumation of Syros and Sifnos metamotphic
881 rocks (Cyclades, Greece). New constraints on the P-T paths. European Journal of
882 Mineralogy 13, 901-920.
883
884 Trullenque, G., Kunze, K., Heilbronner, R., Stünitz, H., Schmid, S.M., 2006.
885 Microfabrics of calcite ultramylonites as records of coaxial and non-coaxial

886 deformation kinematics: Examples from the Rocher de l'Yret shear zone (Western
887 Alps). Tectonophysics 424, 69-97.
888
889 Tullis, J., Yund, R. A., 1982. Grain growth kinematics of quartz and calcite
890 aggregates. Journal of Geology 90, 301-318.
891
892 Vernon, R. H., 1981. Optical microstructure of partly recrystallized calcite in some
893 naturally deformed marbles. Tectonophysics 18, 601-612.
894
895 Wheeler, J. Prior, D. J., Jiang, Z., Spiess, R., Trimby, P. W., 2001. The Petrological
896 significance of misorientations between grains. Contributions to Mineralogy and
897 Petrology 141, 109-124.
898
899 Wortel, M.J.R., Goes, S.D.B., Spakman, W., 1993. Structure and seismicity of the
900 Aegean subduction zone. Terra Nova 2, 554-562.
901
902
903
904
905
906
907
908

Figure Captions

Fig. 1. Schematic sketch of the development of an a-type flanking structure. a. Foliated host rock. b. A crack develops perpendicular to the host-rock foliation. C. Due to shearing the crack (i.e. CE) rotates, resulting in an antithetic offset along the crack. Note that the displacement of marker lines varies along the cross-cutting element (CE) leading to a spatial variation in strain (γ).

Fig. 2. Geological map of Syros (modified after Keiter et al. 2004). The arrow points to the location of the outcrop.

Fig. 3. P-T paths for Syros determined by Trotet et al. (2001), Keiter et al (2004) and Schumacher et al. (2008). LBS=lawsonite-blueshist. EBS=epidot-blueschist, GS= greenschist, A=amphibolite and PA=pumpellyite-actinolite (after Evans, 1990). The black box represents the P-T range of the deformation stage considered in this study.

Fig. 4. a. Sample locations within the outcrop. The inserted sketch shows the deflection of the passive markers (dotted lines). The CE has been retraced by a red line. b. Equal-area, lower hemisphere projection showing the orientation of the cross-cutting element, and the foliation and stretching lineation of the host rock. c. Diagram showing the displacement plotted over the distance along the cross-cutting element with respect to the bottom of the flanking structure. d. Close-up at the boundary of CE and host rock showing a switch from reverse to normal drag at location of the purple line (location shown in Figure 4a).

Fig. 5. Optical micrographs (crossed polarizers). Insets are rose diagrams showing the 2D orientation of the calcite grain long axes. N represents the total number of measured grains and max. the maximal percentage. In all micrographs left side corresponds to W. a. Coarse calcite grains (low-strain domain, sample 1) of the host

933 rock showing a weak undulatory extinction and a SPO with an angle of 40° relative to
934 the foliation. Locally sutured grain boundaries occur whereas twins are preferentially
935 straight and thin. b. Coarse calcite grains of the host rock (low-strain domain, sample
936 3a) showing undulatory extinction and sutured grain boundaries. Note that the grains
937 have been rotated with respect to the cross-cutting element leading to an alignment
938 parallel to the foliation. c. Equigranular, recrystallized calcite ultramylonite next to
939 protomylonite (intermediate-strain domain, sample 2). d. Protomylonitic calcite
940 showing a core-mantle structure with strongly deformed host grains surrounded by
941 recrystallized grains (intermediate-strain domain, sample 2). e. Equigranular,
942 recrystallized calcite ultramylonite (high-strain domain, sample 3b). f. Fine grained
943 ultramylonite layer (high-strain domain, sample 3b). g. Core-mantle structures
944 showing that subgrains and recrystallized grains have the same size (intermediate-
945 strain domain). White arrows point to location of subgrains and recrystallized grains.
946 h. Close-up of ultramylonitic calcite (intermediate-strain domain). i. Core-mantle
947 structure showing that subgrains and recrystallized have a similar size (high-strain
948 domain). White arrows point to the location of subgrains and recrystallized grains. j.
949 Close-up of ultramylonitic calcite (high-strain domain). k. Boundary between
950 ultramylonitic and fine-grained ultramylonitic calcite. Presence of fine grained
951 ultramylonite layer amongst mylonitic grains. Note the small bulges and triple
952 junctions (arrows). l. Close-up of fine grained ultramylonitic layer.

953 **Fig. 6.** Optical micrographs of mica (crossed polarizers). In all micrographs left side
954 corresponds to W. a. Mica in protomylonitic layer aligned parallel to the cross-cutting
955 element boundary. b. Mica in mylonitic layer aligned parallel to long axes of
956 recrystallized grains.

957 **Fig. 7.** Grain-size histograms of dominant microstructures of low-strain (a.),
958 intermediate-strain (b., c., d., e.) and high-strain domains (f., g., h., i., j.). Note that
959 recrystallized grains of protomylonitic layers and ultramylonitic layers have almost the
960 same grain size distribution. N= total number of analysed grains, d= mean grain size,
961 s= standard deviation.

962 **Fig. 8.** Stereographic equal-area upper hemisphere projection of c (0001), -a <11-
963 20>, a <-1-120> axes and r planes {10-14} of calcite. z, y and x show the sample
964 axes, the black line (F) represents the foliation and the red line (CEB) the cross-
965 cutting element boundary. a. Host rock (low strain domain, sample 1). b. Host rock
966 next to cross-cutting element (low strain domain, sample 3a). c. Host grains of
967 protomylonitic layer (intermediate-strain domain, sample 2). d. Recrystallized grains
968 of protomylonitic layer (intermediate-strain domain, sample 2). e. Recrystallized
969 grains of mylonitic layer (intermediate-strain domain, sample 2). f. Host grains of
970 protomylonitic layer (high-strain domain, sample 3b). g. Recrystallized grains of
971 protomylonitic layer (high-strain domain, sample 3b). h. Recrystallized grains of
972 mylonitic layer (high-strain domain, sample 3b). i. recrystallized grains in
973 ultramylonitic layer (high-strain domain, sample 3b).

974 **Fig. 9.** Misorientation angle distribution plots of dominant microstructures in low- (a.),
975 intermediate-(b., d.) and high-strain domains (c., e., f.). N represent the total number
976 of analysed grains.

977 **Fig. 10.** Table of microfabric characteristics of low-, intermediate- and high strain
978 domains. Data in the first row have been mirrored with respect to the corresponding
979 thin section in order to display all data in the same reference frame.

980 **Fig. 11.** Recrystallized grain-size evolution in the low-strain (green), intermediate-
981 strain (yellow) and high-strain (orange) domains plotted in a grain-size- vs.
982 differential-stress deformation-mechanism map for calcite at 300 °C. Additionally the
983 calcite paleowattmeter (Austin and Evans, 2009), the calcite paleopiezometers
984 (Schmid, 1980; Rutter, 1995) and the viscosities for the corresponding mean grain
985 sizes are given with the logarithmic scale. Flow laws by Renner et al. (2002) for GSI
986 and Herwegh et al. (2003) for GSS creep. The isolines represent constant strain
987 rates.

988

989

990

991

992

993

994

995

996

997

998

999

1000

Appendix

A1.

For the calculation of the deformation mechanism map, we used the composite flow law after Ter Heege et al. (2004). The diffusion creep field was calculated applying the flow law by Herwegh et al. (2003) that represents a combination of diffusion creep and grain-boundary sliding

$$\dot{\gamma}_{GSS} = A\sigma^{n}d^{-m}\ exp(-Q/R/T), \quad \text{Eq. 3}$$

with $n=1.1$, $m=3.3$, an activation energy Q=200 kJ/mol and A= 4.3x10^{7}.

For the dislocation creep field, we used the flow law by Renner et al. (2002) that is well suited for low-temperature data (De Bresser et al., 2002).

$$\dot{\gamma}_{GSl} = A\sigma^{n}\ exp(\sigma/\sigma_{0})\ exp(-Q/R/T), \quad \text{Eq. 4}$$

with $n=2$, Q= 200 kJ/mol and A= 270. σ_0 calculated by the formula

$$\sigma_{0} = (\sigma+115\ d^{-0.5})\ (T_m-T)/1000, \quad \text{Eq. 5}$$

where T_m is the melting temperature and d the grain size.

Stresses were calculated with the paleopiezometer of Rutter (1995) for subgrain rotation recrystallization

$$\sigma = 10^{2.91} * d^{-0.88}, \quad \text{Eq. 6}$$

and for grain-boundary migration recrystallization

$$\sigma = 10^{3.43} * d^{-0.89}, \quad \text{Eq. 7}$$

and the paleopiezometer of Schmid (1980)

$$\sigma = 10^{2.69} * d^{-1.02}, \quad \text{Eq. 8}$$

In all equations, σ is the differential stress and $\dot{\gamma}$ the strain rate, R represents the gas constant and T the deformation temperature in K.

A2.

In this appendix, we derive a relationship between the amount of finite strain and the kinematic vorticity number for the outcrop. Isovolumetric plane strain is assumed so that the finite strain tensor within the shear zone reference framework can be written as a function of two positive unknown parameters: the longitudinal strain along the shear zone, k, and the shear strain along the shear zone, Γ

$$D = \begin{bmatrix} k & \Gamma \\ 0 & 1/k \end{bmatrix} \quad \text{Eq. 9}$$

The crosscutting element formed as a crack initially perpendicular to the foliation plane, which is assumed to be parallel to the stretching eigenvector of finite strain (Fig.A1a). In the Mohr space, the initial direction the crack corresponds to the point CE and the direction of the stretching eigenvector corresponds to the point A_1. Since these directions were initially perpendicular, A_1 and CE are opposite points on the same diameter of the finite-strain Mohr circle of second kind (De Paor and Means, 1984; Fig.A1b). There coordinates are respectively A_1: (0, k) and CE: (Γ, 1/k).

The crosscutting element has rotated by an angle β that we can deduce form field measurements of the angle between the rotated crosscutting element and the

foliation plane. Therefore, the point CE is at the intersection between the finite strain Mohr circle and the line $x = y \tan \beta$ (Fig.A1b). This gives us a relationship between k and Γ:

$$\Gamma = tan\,\beta/k \qquad \text{Eq. 10}$$

so that the coordinates of point CE are $(\tan \beta/k,\ 1/k)$. They are used for calculating the diameter of the finite-strain Mohr circle as the distance between points A_1 and CE:

$$d = \frac{\sqrt{tan^2\beta+(k^2-1)^2}}{k} \qquad \text{Eq. 11}$$

The diameter of the finite-strain Mohr circle is used as a proxy for strain in general shear since it is exactly equal to Γ in simple shear and it is equal to $k - 1/k$ in pure shear.

Using geometry of the finite-strain Mohr circle, we can determine the coordinates of the center of the Mohr circle C: $(\tan\beta/2k,\ (k^2+1)/2k)$ and the point corresponding to the shortening finite strain eigenvector A_2 : $(0,\ 1/k)$.

The angle between the two eigenvectors in the Mohr space is 2α, where α is the angle between the two eigenvectors in the physical space. The value of $\cos 2\alpha$ can be calculated using a scalar product in the Mohr space between the vectors CA_1 and CA_2 divided by their norms:

$$cos2\alpha = \frac{tan^2\beta-(k^2-1)^2}{tan^2\beta+(k^2-1)^2} \qquad \text{Eq. 12}$$

where equation 11. has been used for calculating the norms of the vectors. The kinematic vortocity W_k is then calculated following Bobyarchick (1986)

$$W_k = cos\alpha = \sqrt{\frac{1+cos2\alpha}{2}},$$

$$= \sqrt{\frac{tan^2\beta}{tan^2+(k^2-1)^2}} \quad \text{Eq. 13}$$

Finally, even though the value of k remains unknown (i.e. the Mohr circle is not scaled), it is possible to plot the diameter of the finite-strain Mohr circle in an equation as a function of the kinematic vorticity. Equation 13 is used for calculating:

$$(k^2-1)^2 = \frac{tan^2\beta}{W_k^2} - tan^2\beta \quad \text{Eq. 14}$$

and

$$k = \sqrt{1 + tan\beta\sqrt{1/W_k^2 - 1}} \quad \text{Eq. 15}$$

Equations 13 and 14 are introduced into equation 11:

$$d = \frac{tan\beta}{Wk\sqrt{1+tan\beta\sqrt{1/W_k^2-1}}} \quad \text{Eq. 16}$$

Figure A1c represents the graph of d as a function of W_k using the average value of the cross-cutting element rotation: $\beta = 70°$. It shows that the bulk strain in the shear was less than 3, if the kinematic vorticity number was larger than 0.29. Therefore, even if the pure shear component responsible for the observed deformation was large, the amount of bulk strain was most likely limited to values comprised between 2 and 3. Larger values of bulk strain would have “erased” the flanking structure.

Figure1

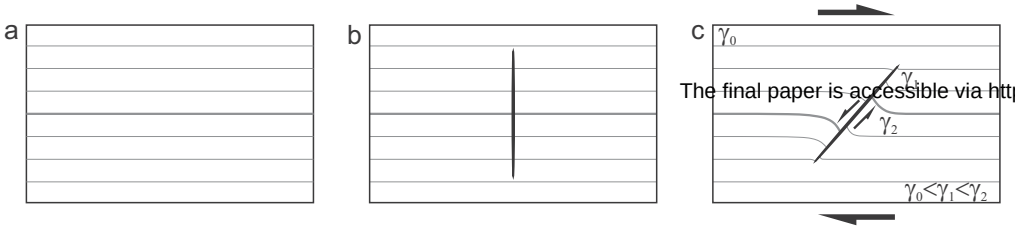

Fig.1

Figure2

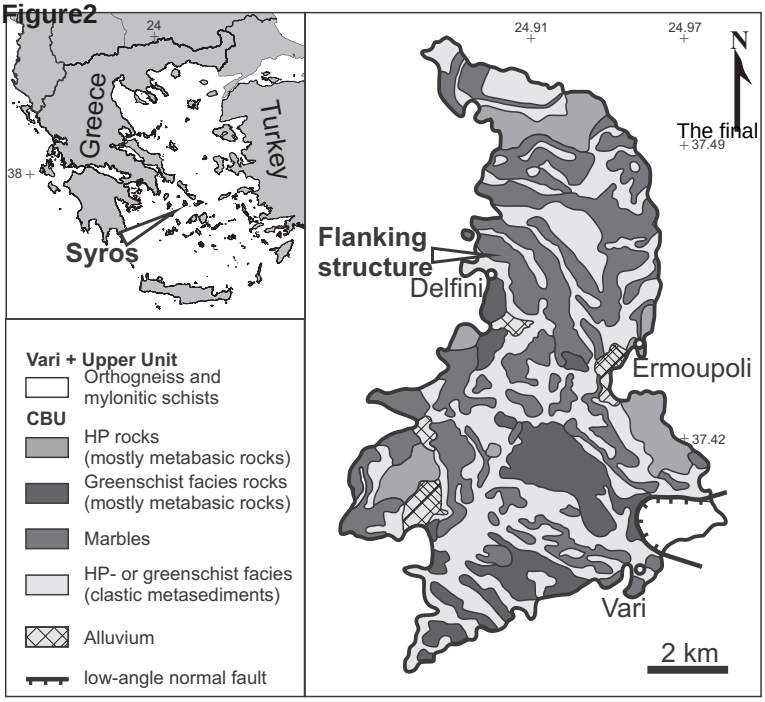

Fig.2

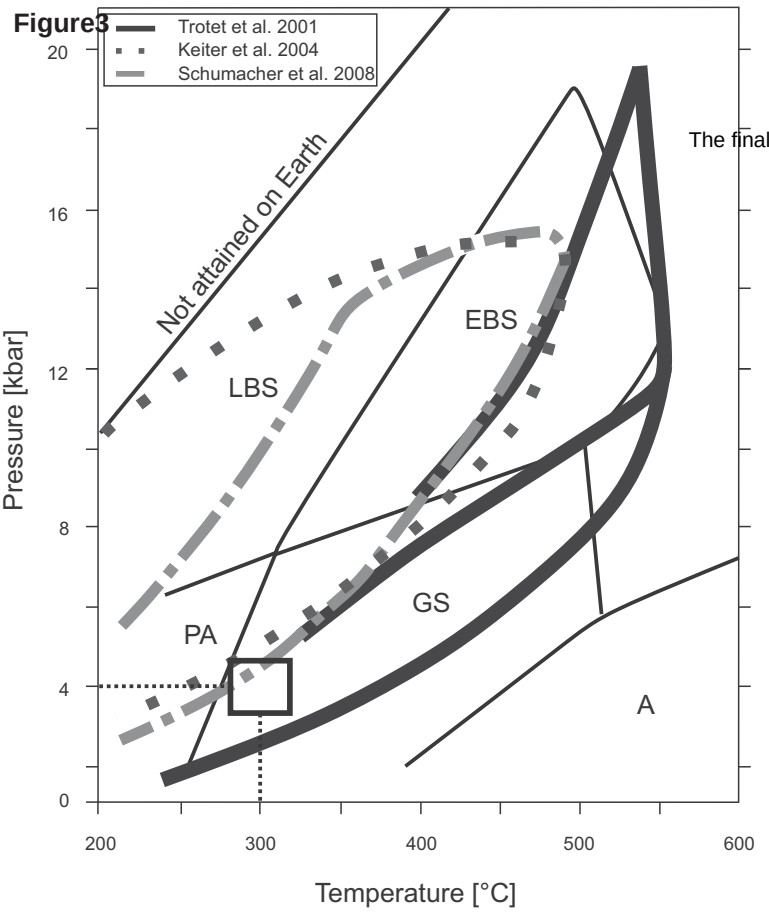

Fig. 3

Figure4

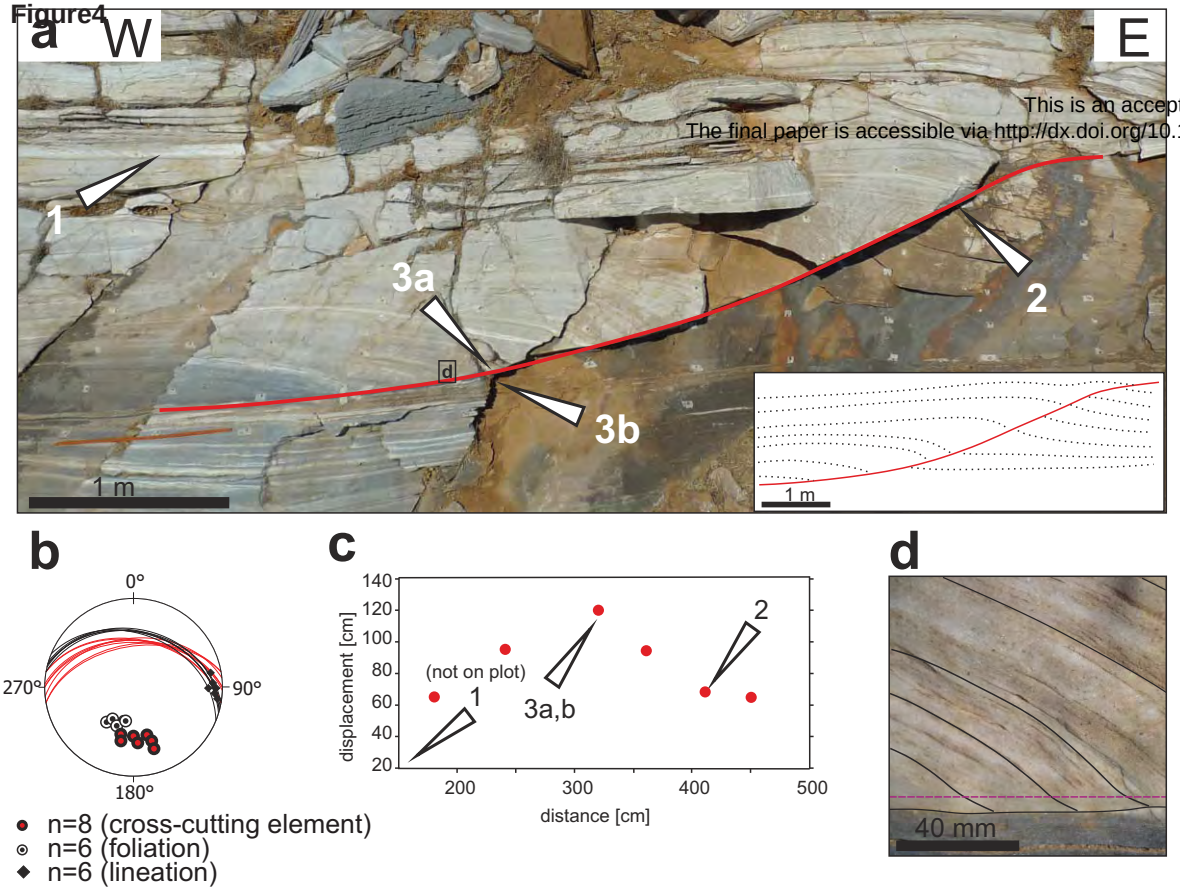

Fig.4

Figure5

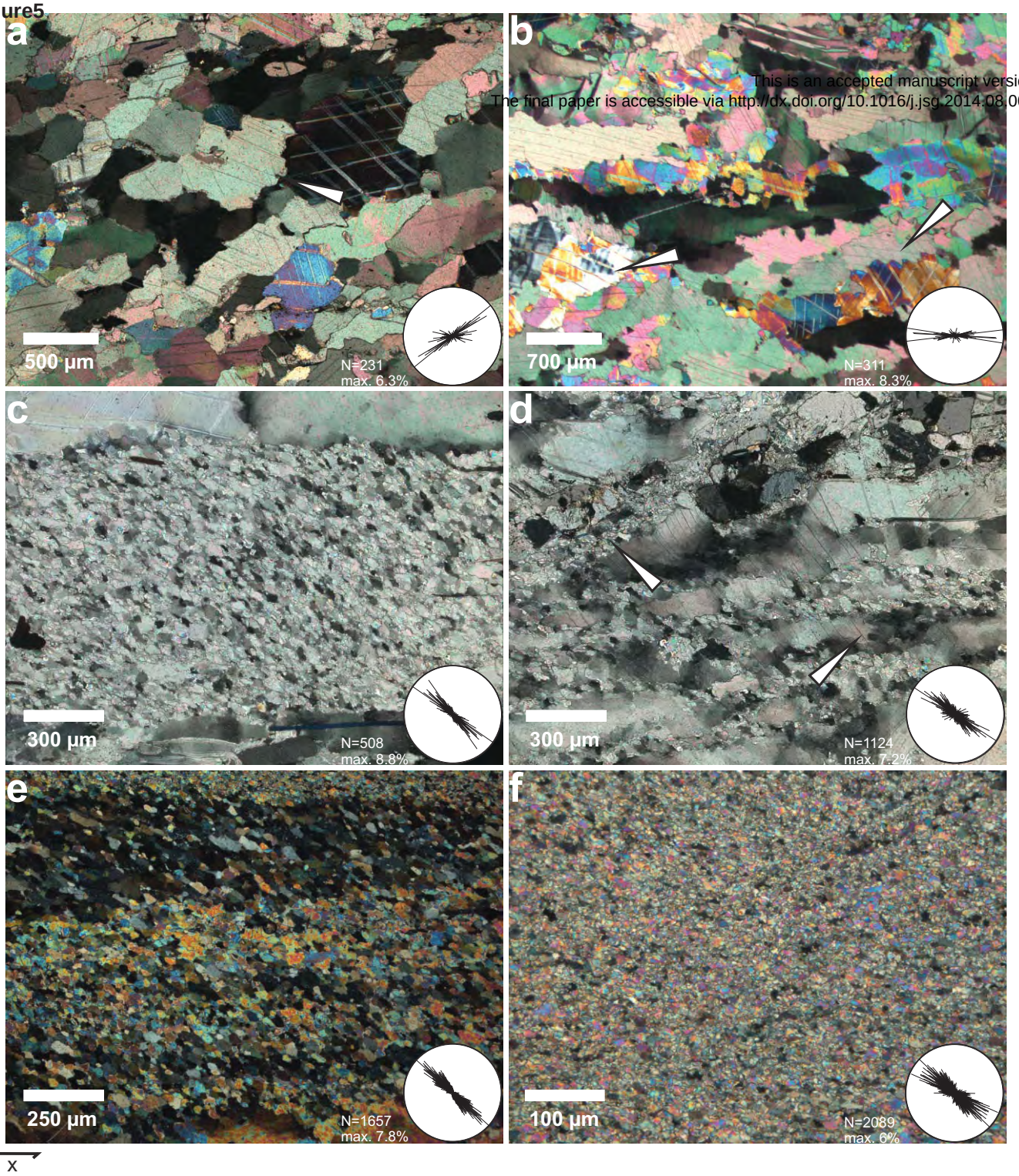

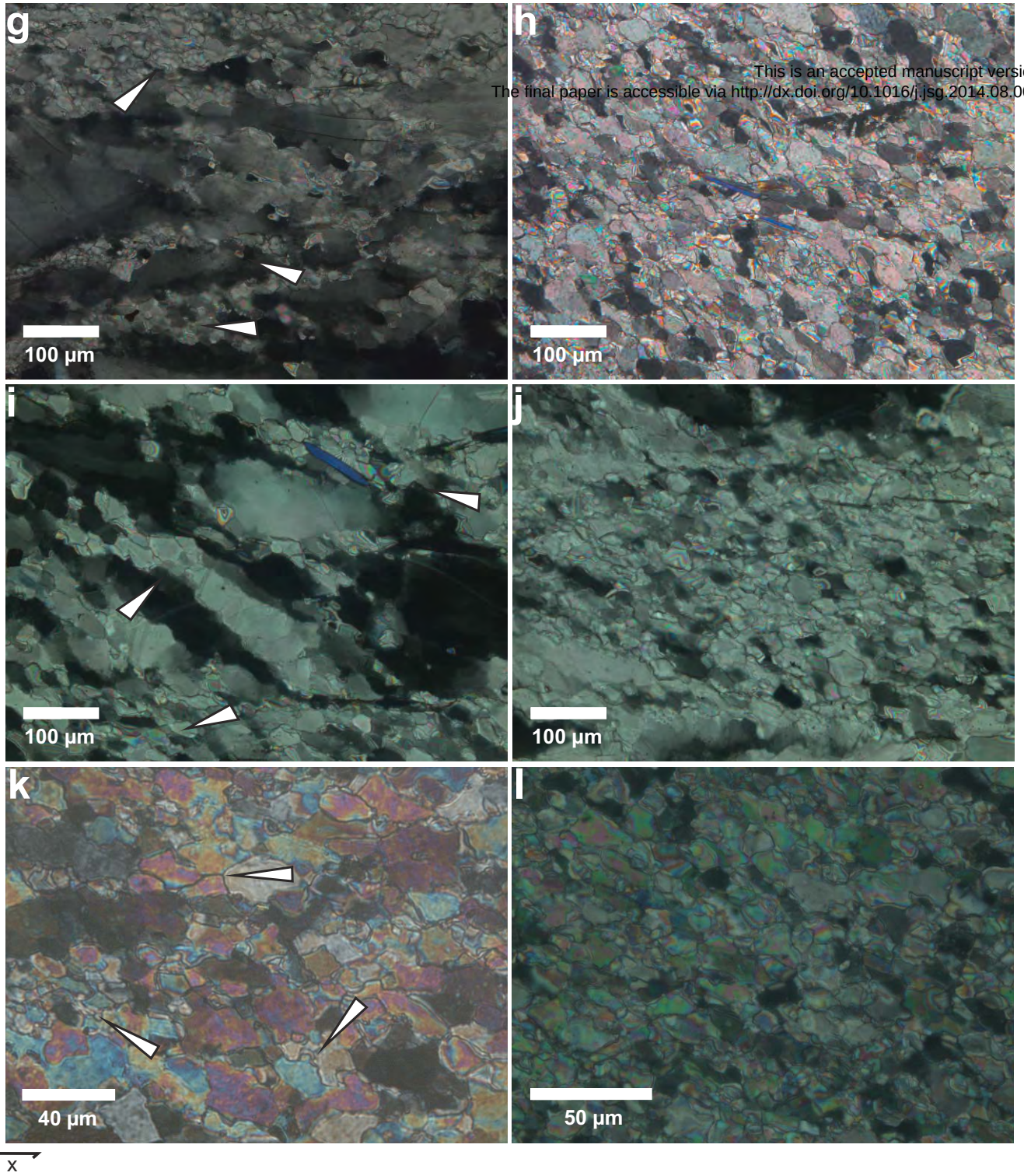

Fig.5

Figure6

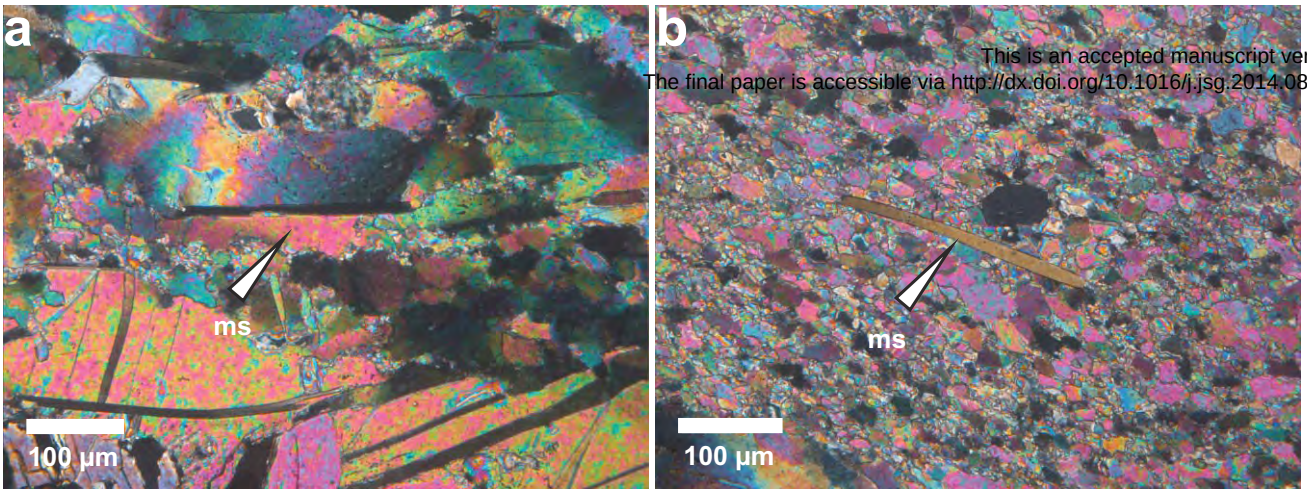

Fig.6

Figure7

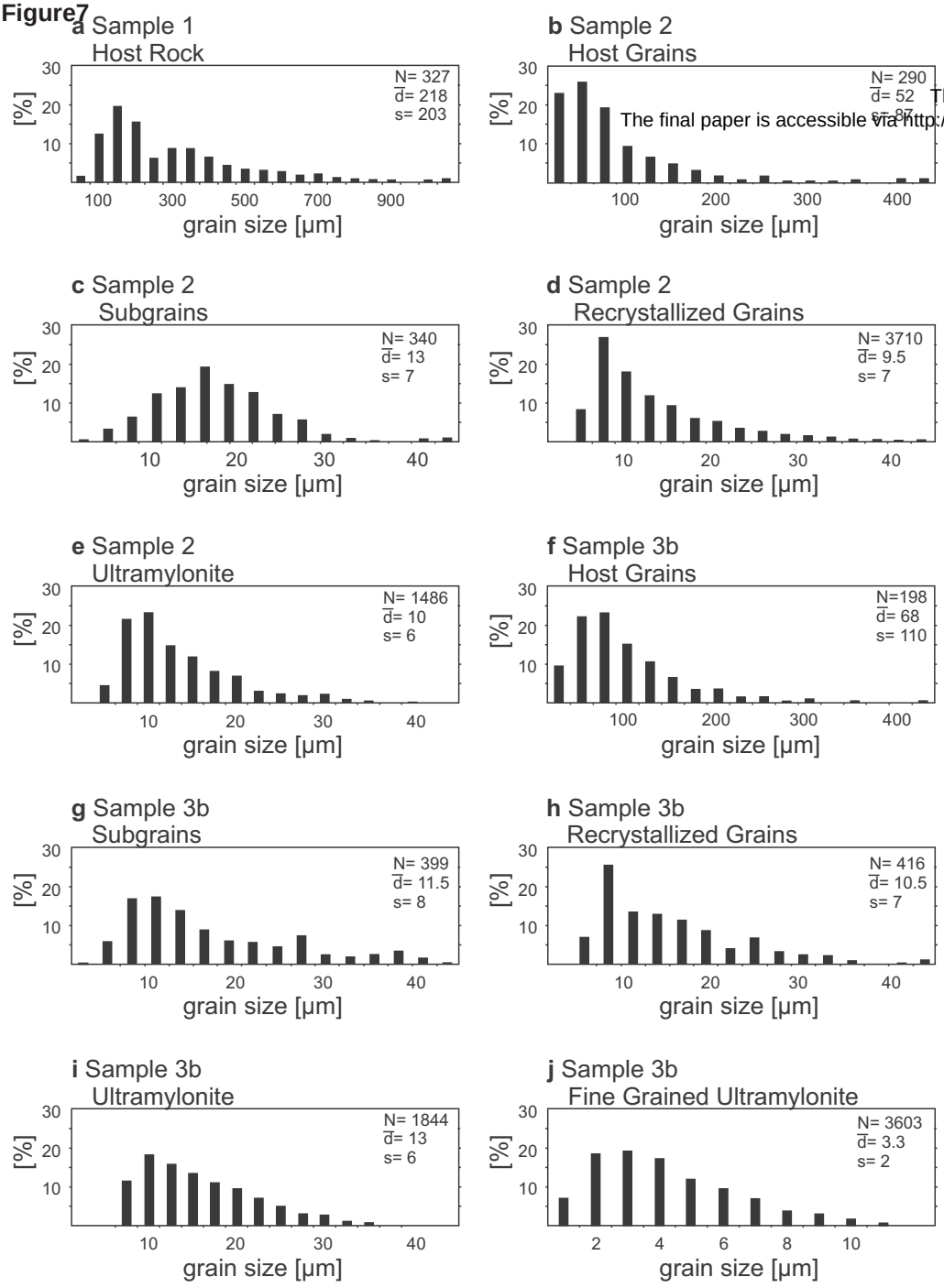

Fig.7

Figure8

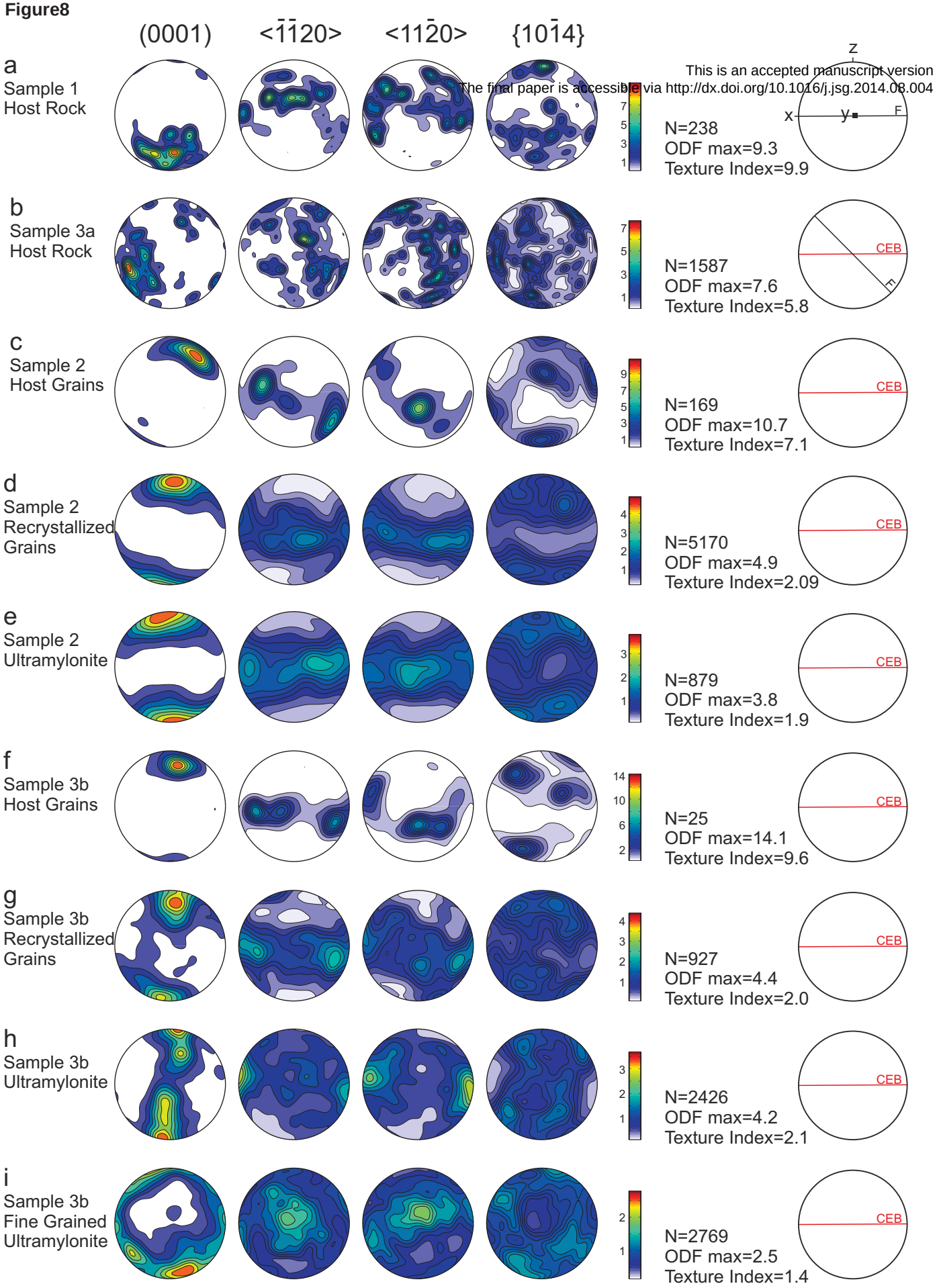

Fig.8

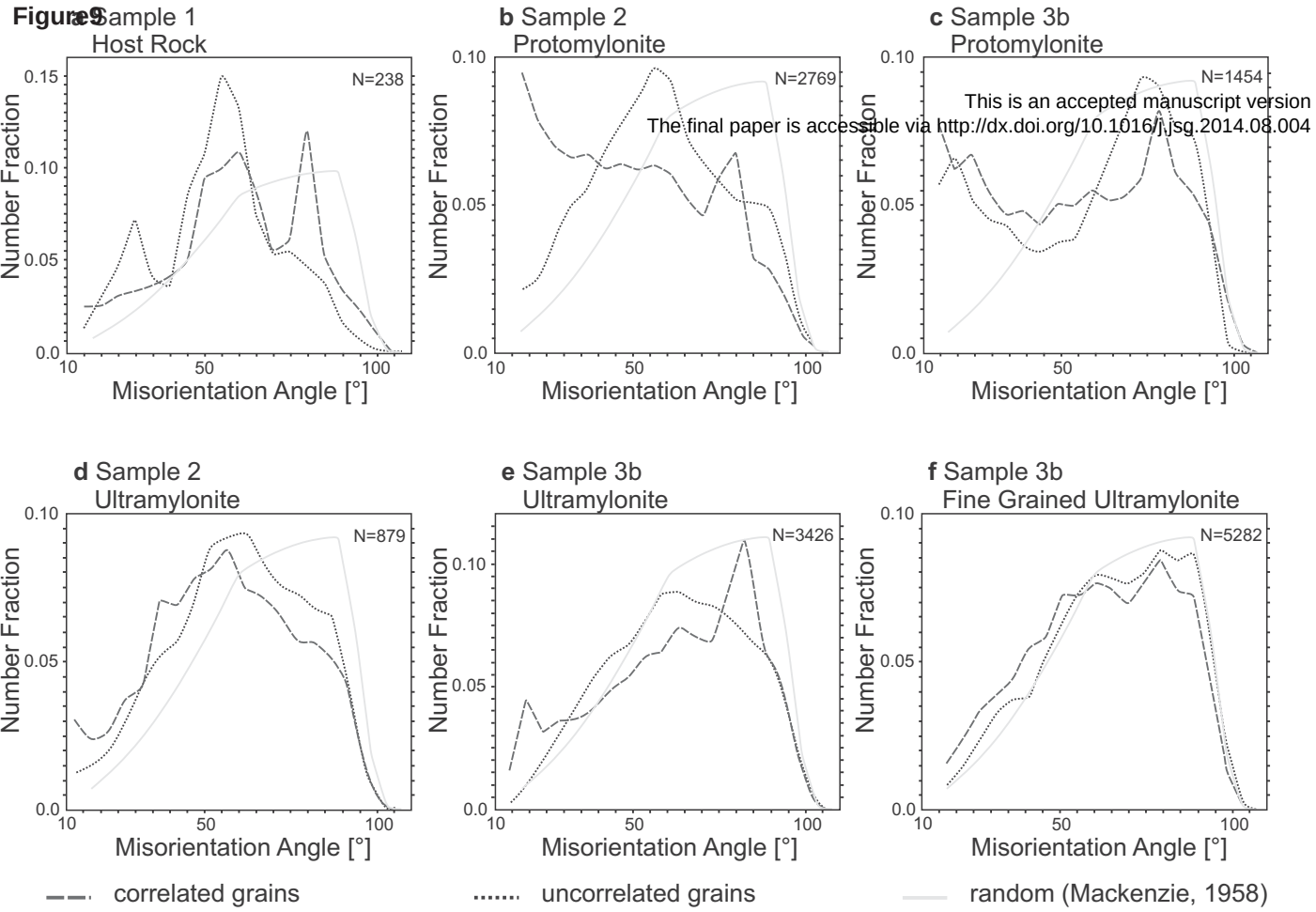

Figure 9

Fig.9

Figure10

microstructure	average grain size	deformation mechanism	SPO recrystallized grains	c axis orientation	strain rate
	218 μm	dislocation creep (GBM)			$\dot{\gamma}=10^{-12.5}\,s^{-1}$
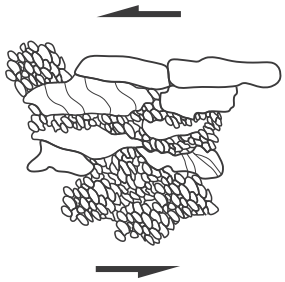	52 μm	twinning, dislocation creep		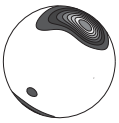	$\dot{\gamma}=10^{-11.5}\,s^{-1}$
	10 μm	dislocation creep (SGR)			$\dot{\gamma}=10^{-11.5}\,s^{-1}$
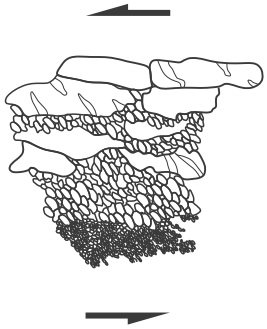	68 μm	twinning, dislocation creep			$\dot{\gamma}=10^{-10.5}\,s^{-1}$
	13 μm	dislocation creep (SGR)			$\dot{\gamma}=10^{-10.5}\,s^{-1}$
	3.3 μm	(BLG) GBS			$\dot{\gamma}=10^{-9.5}\,s^{-1}$

Fig.10

Figure11

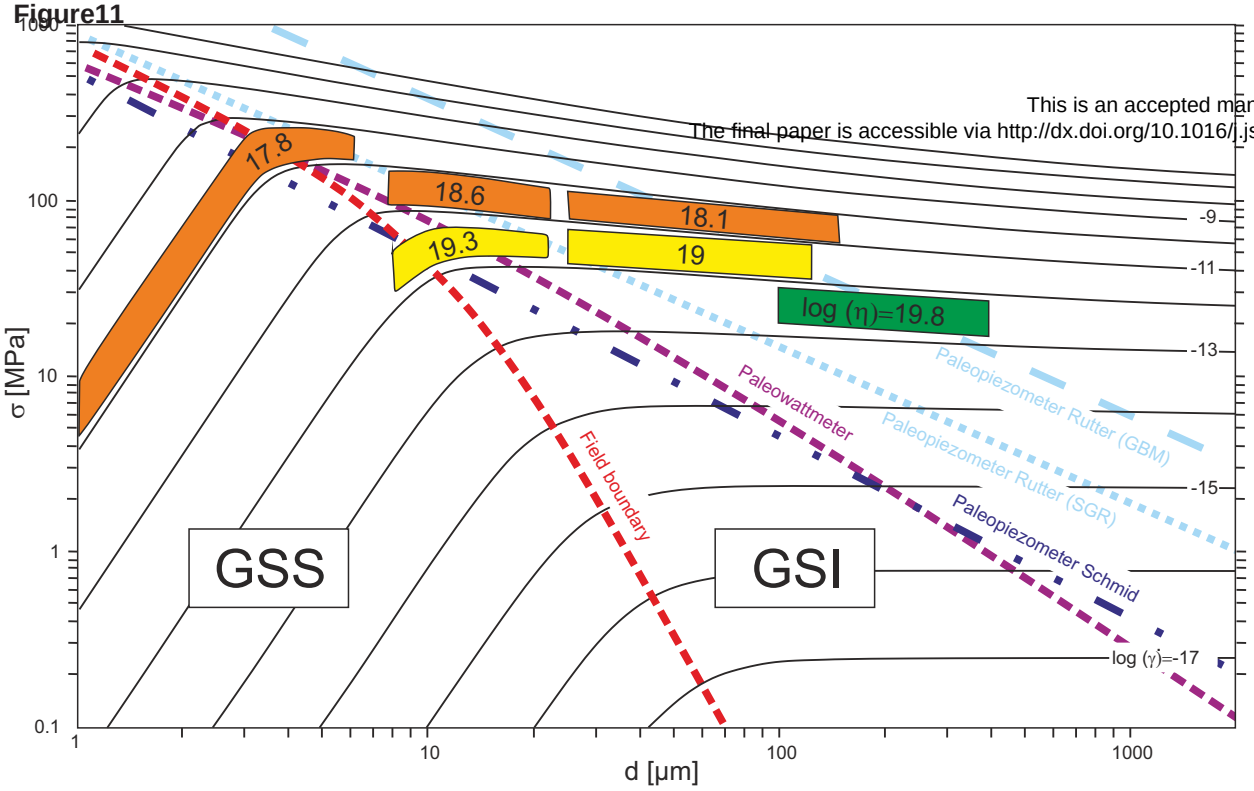

Fig.11

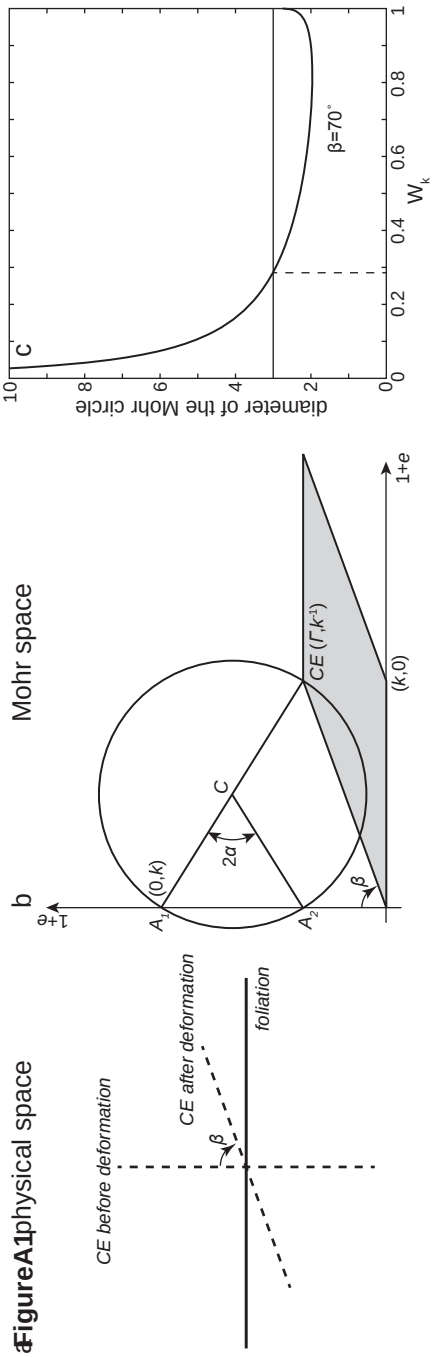

FigureA1

supplementary material

Click here to download Supporting Material: flanking_structure_syros.pdf